Supplement to:

CCN activity and organic hygroscopicity of aerosols downwind of an urban region in central Amazonia: Seasonal and diel variations and impact of anthropogenic emissions

Ryan Thalman[1,#], Suzane S. de Sá[2], Brett B. Palm[3], Henrique M. J. Barbosa[4], Mira L. Pöhlker[5], M. Lizabeth Alexander[7], Joel Brito[4*], Samara Carbone[4], Paulo Castillo[1], Douglas A. Day[3], Chongai Kuang[1], Antonio Manzi[8], Nga Lee Ng[9,10], Arthur J. Sedlacek III[1], Rodrigo Souza[11], Stephen Springston[1], Thomas Watson[1], Christopher Pöhlker[5], Ulrich Pöschl[5,6], Meinrat O. Andreae[5,12], Paulo Artaxo[4] Jose L. Jimenez[3], Scot T. Martin[2,13], Jian Wang[1]

[1]Environmental and Climate Sciences Department, Brookhaven National Laboratory, Upton, NY, USA

[2]School of Engineering and Applied Sciences, Harvard University, Cambridge, MA, USA

[3]Department of Chemistry and Biochemistry and Cooperative Institute for Research in Environmental Sciences (CIRES), University of Colorado Boulder, Boulder, CO, USA

[4]Physics Institute, University of São Paulo, São Paulo, Brazil

[5]Biogeochemistry and Multiphase Chemistry Departments, Max Planck Institute for Chemistry, Mainz, Germany

[6]Scripps Institution of Oceanography, University of California San Diego, La Jolla, CA, USA

[7]Pacific Northwest National Laboratory, Richland, WA, USA

[8]National Institute of Amazonian Research, Manaus, Amazonas, Brazil

[9]School of Chemical and Biomolecular Engineering, Georgia Institute of Technology, Atlanta, GA, USA

[10]School of Earth and Atmospheric Sciences, Georgia Institute of Technology, Atlanta, GA, USA

[11] Amazonas State University, Manaus, Amazonas, Brazil

[12]Scripps Institution of Oceanography, University of California San Diego, La Jolla, CA, USA

[13]Department of Earth and Planetary Sciences, Harvard University, Cambridge, MA, USA

[#]Now at Department of Chemistry, Snow College, Richfield, UT, USA

[*]Now at Laboratory for Meteorological Physics, University Clermont Auvergne, Clermont-Ferrand, France

Correspondence to: J. Wang (jian@bnl.gov)

1 Calibration and Operation of the CCN counter

The system used to measure size-resolved CCN spectra during GoAmazon 2014/5 is shown in Fig. S1, and the operation sequences of DMA classified particle diameter, Q_{CCN} and ΔT are present in Fig. S2. The CCN counter was calibrated at each flow and temperature setting using ammonium sulfate as an inorganic aerosol standard (Lance et al., 2006; Mei et al., 2013; Roberts and Nenes, 2005; Shilling et al., 2007). As the temperatures at the top of the CCN counter column (T_1) varies with room temperature, the calibration was repeated for each pair of Q_{CCN} and ΔT over a range of T_1 typically encountered during GoAmazon 2014/5. The calibration results are shown as a function of Q_{CCN} and ΔT conditions at $T_1 = 25°C$ in Fig. S3, and the variation of instrument supersaturation (SS) with respect to T_1 is present in Fig. S4. Instrument supersaturation during the measurements was calculated using the Q_{CCN}, ΔT, and T_1 based on the calibrations.
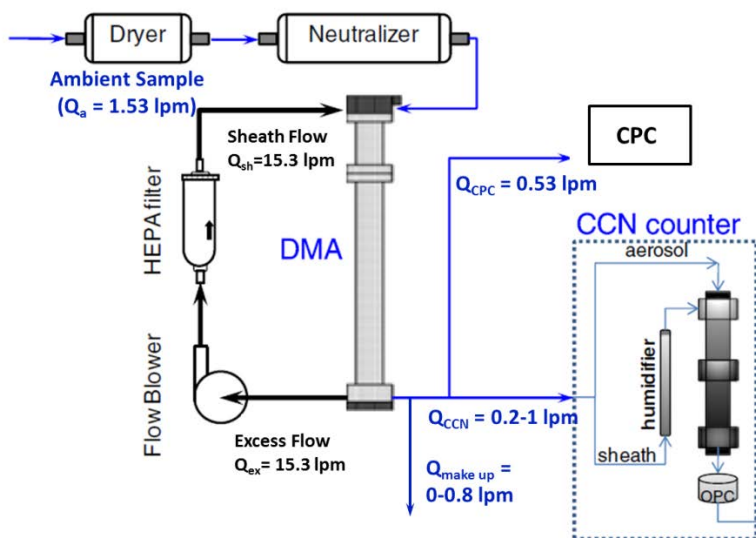
Figure S1: Schematic of the system for measuring size-resolved CCN spectra during GoAmazon 2014/5.

52   .
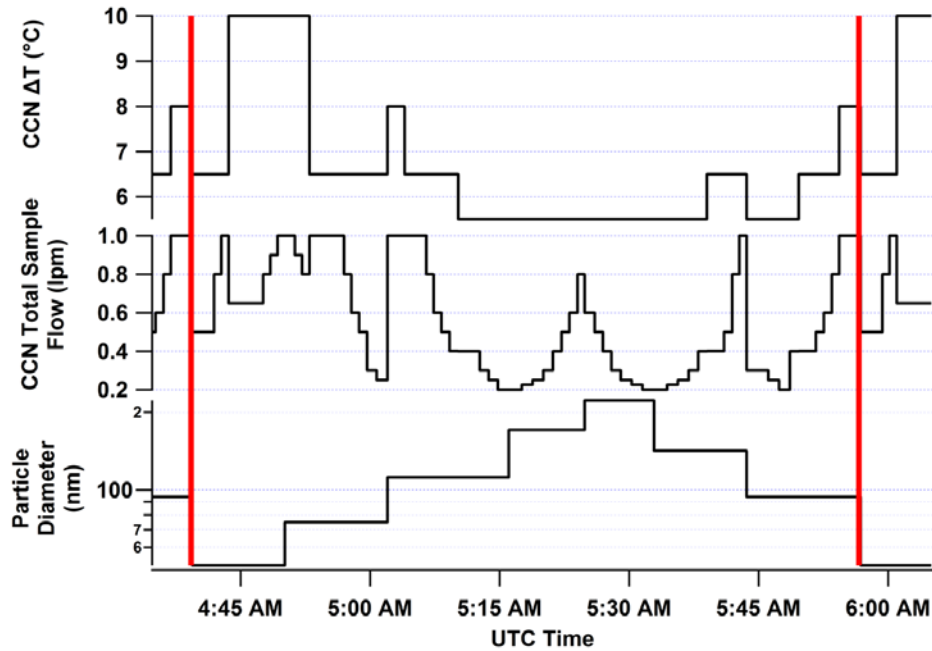
Figure S2: Instrument operation sequence showing set points of DMA classified particle
diameter, Q_{CCN} and ΔT for one full measurement cycle. Red vertical lines mark the start and
finish of one cycle.
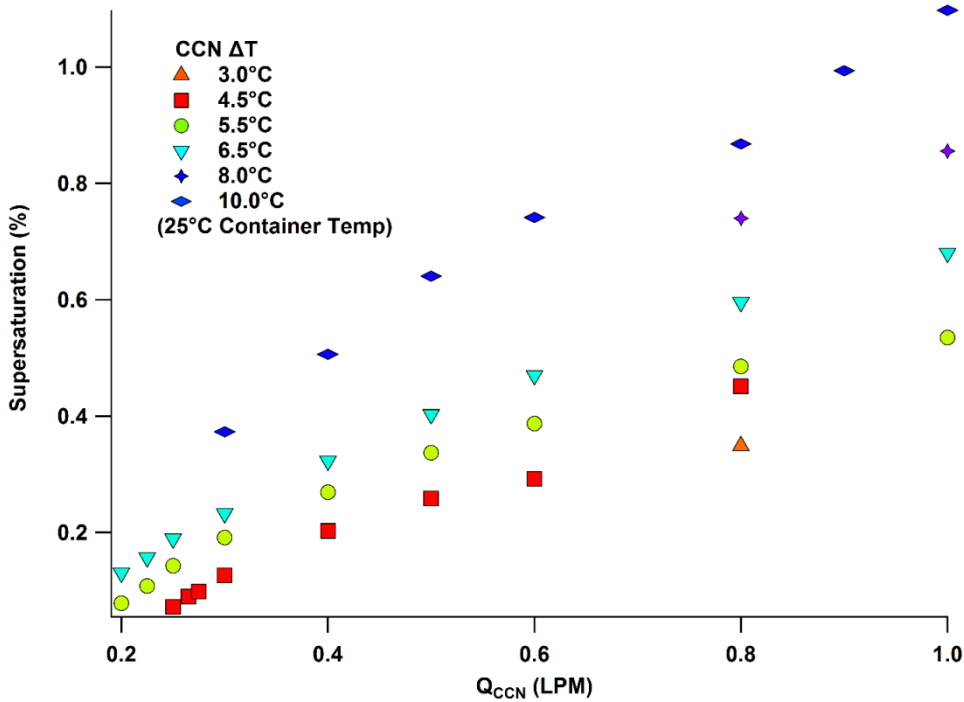
Figure S3: Calibrated CCN counter supersaturation as a function of ΔT at T_1 of 25°C for Q_{CCN}
ranging from 0.2 to 1.0 LPM.

59
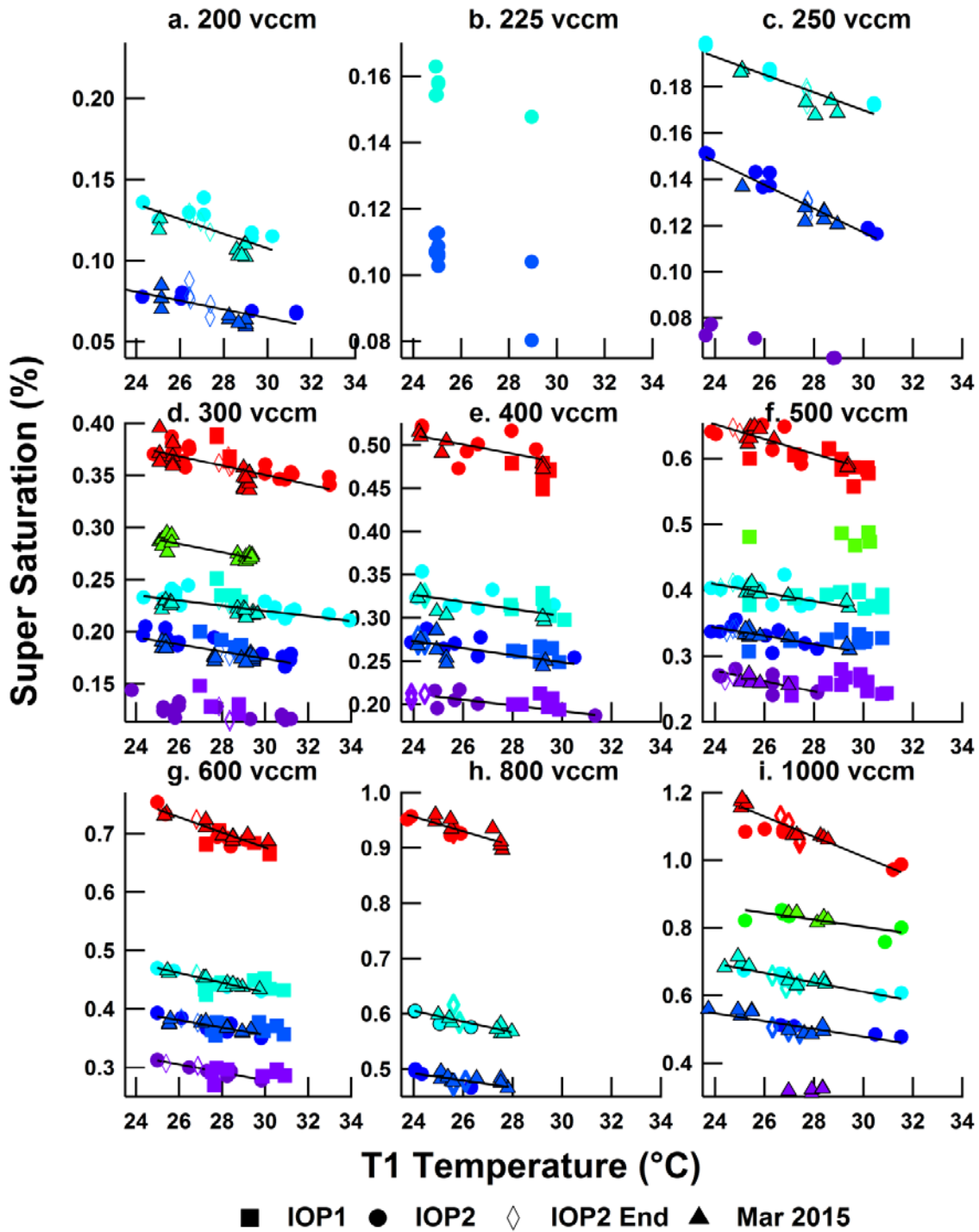
Figure S4: Calibrated instrument supersaturation as a function of T_1 for different ΔT and Q_{CCN} values. The symbol colors of purple, dark blue, light blue, green and red correspond to ΔT values of 4.5, 5.5, 6.5, 8.0, and 10.0°C, respectively. Calibrations were carried out throughout the entire campaign (February/March 2014 - ■; August 2014 - ●; October 2014 - ◊; March 2015 - ▲). The lines represent least square fits of the calibration results.

2 ARM Facility Instruments

2.1 Measurements of Oxides of Nitrogen

Oxides of nitrogen were measured by catalytic conversion to NO and chemiluminescence at one minute time resolution. The $NO/NO_2/NO_y$ system is based on two Thermo Scientific 43i instruments and customized by Air Quality Design, Inc. (Wheatridge, CO) for detection of NO. The inlet/converter box is external and located at 10 meters above ground level and is environmentally controlled. A dedicated channel converts total NOy ($NO + NO_2 + HNO_3$ + peroxy acyl nitrates + aerosol nitrates, but not NH_4) to NO via a Mo catalyst heated to 325°C. A second channel converts NO_2 to NO by a light emitting diode (LED) photolysis cell with 50% conversion efficiency (C.E.). The LED is toggled on and off on a two minute cycle to measure ambient NO and NO + C.E.× NO_2, and the NO_2 mixing ratio is derived from the difference of the measurements. The inlet box contains mass flow controllers (MFCs) so that the residence time to the chemiluminescence cells is minimal and occurs at reduced pressure. The unit is calibrated daily with standard additions of NO and NO_2 to measure the conversion efficiency of both the Mo converter (1.00±0.02) and the photolysis cell.

2.2 Refractory Black Carbon Measurements

The incandescence signal measured by SP2 is proportional to the mass of rBC in the particles irrespective of whether the rBC is coated or not (Moteki et al., 2007; Schwarz et al., 2010; Stephens et al., 2003). The SP2 was calibrated using size-selected fullerene soot with no corrections for non-rBC content. The detectable size range of the SP2 is 75 – 600 nm (volume equivalent diameter), which typically provides a direct measurement of > 90% of rBC mass concentrations. If necessary, the complete mass size distribution is extrapolated to include rBC outside of this size range assuming a log-normal distribution (Mei et al., 2013a). During

88   GoAmazon 2014/5, rBC mass was mostly within the detectable range. In contrast to the SP2, the

89   seven-wavelength Aethalometer (Arnott et al., 2005; Hansen et al., 1984) reports an equivalent

90   black carbon mass loading by converting a light absorption measurement from aerosols

91   accumulated on a filter relative to a manufacturer-supplied conversion. However, there is

92   substantial and growing evidence relating to measurement artifacts attributed to aerosol loading

93   effects and enhanced light absorption through multiple-scattering of photons (Collaud Coen et

94   al., 2010; Rizzo et al., 2011; Schmid et al., 2006; Virkkula et al., 2015; Virkkula et al., 2007;

95   Weingartner et al., 2003). Given the more complete dataset of the Aethalometer, our analysis

96   utilized the Aethalometer data only when SP2 data was unavailable. The available concurrent

97   SP2 and Aethalometer datasets were used to derive a linear relationship to correct for

98   Aethalometer measurement artifacts cited above. The mass concentrations of refractory black

99   carbon (rBC) derived from SP2 and Aethalometer data were averaged to a common time base

100 and the least square linear fit between both rBC mass concentrations is shown in Fig. S5 for both

101 the wet and dry seasons. The linear relationship exhibited a seasonal dependence, which might

102 be driven by variations in RH, the ratio of mass concentrations of organics to BC, or a

103 combination of both. The rBC mass concentration derived from the Aethalometer measurement

104 was used to fill the gaps in the SP2 data after scaled using the linear relationship corresponding

105 to the respective season.

106

107
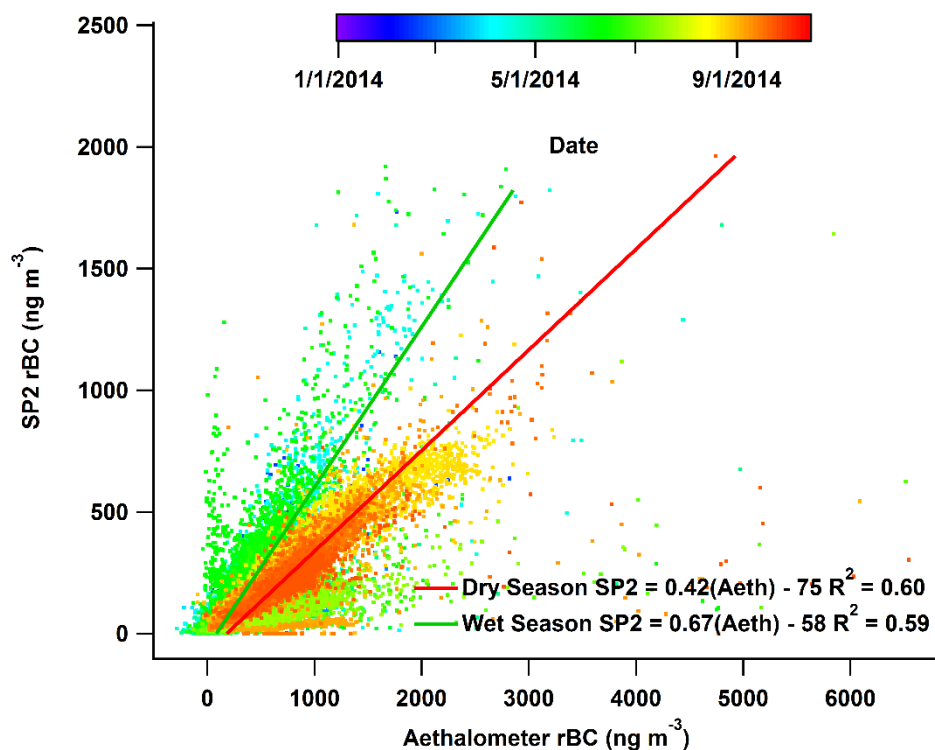
Figure S5: Correlation between rBC mass concentrations derived from the Aethalometer and SP2 measurements. Data points are colored by the time of the measurements. The red and green lines represent least square fit of data collected during the dry and wet seasons, respectively.

3 Reduction of the size resolved CCN activation spectrum

3.1 Correction for multiple charging

Size-resolved CCN activation fraction was characterized at particle diameters of 51, 75, 94, 112, 142, 171 and 222 nm. These sampling sizes were selected to form a progression of particle diameters corresponding to doubly and triply charged particles (e.g. 112 nm corresponds to the diameter of doubly charged particles, when the DMA is set to select particles with a diameter of 75 nm. See Table S1 for more details). The contribution of doubly and triply charged particles to the activation fraction was corrected using the size distribution measured by the SMPS (Model 3080 TSI, Inc) in MAOS and particle charging probabilities (Wiedensohler, 1988). In cases when the size distribution data were not available, we used the concentrations of classified

123   particles measured by the CPC in the size-resolved CCN system when sampling at corresponding

124   multiple-charged sizes. The impact of multiple-charged particles on activation fraction was then

125   accounted for using the concentration of multiple-charged particles and the measured activation

126   fractions at the corresponding sizes. This is similar to the methods established in the literature

127   (Rose et al., 2008). When direct measurements of the activation fraction of multiple charged

128   particles were not available, the multiple charged particles were assumed to have the same

129   distribution of κ as the singly charge particles, and the activation fraction was corrected using the

130   following iterative approach. First, the activation fractions of multiple charged particles were

131   derived from the measured activation factions, taken into consideration the same κ distribution

132   but larger particle diameters. These derived activation fractions at multiple charged sizes were

133   then used to correct measured activation fraction using the approach described above. This

134   process was continued until the corrected activation fraction of singly charged particles

135   converged.

136

137   **3.2 Data quality control criteria**

138   Several quality-control criteria were applied to the data and results from the fitting of

139   activation spectrum. The measurement of the entire activation spectrum at a single particle

140   diameter took about 5-20 minutes. Individual points (i.e., activation fraction at a single S) of an

141   activation spectrum were excluded from the fitting if the standard deviation of 1-sec

142   measurements of the classified particle concentration is greater than 30% of the mean value for

143   the current size, or single data points are more than 1.5 times the mean. This is to remove large

144   fluctuation or spikes in CPC concentration due to contamination by emission of site generator or

145   traffic. The removal of measurement at single supersaturation typically does not prevent fitting

146   of the activation spectrum using data at remaining supersaturation points. Parameters derived

147   from the fitting of activation spectrum were flagged and excluded from further analysis in this

148   study for the following scenarios:

149   1. The fitted $S*$ is outside the supersaturation range of the measured activation spectrum.

150   2. The fitted maximum activated fraction (E) is not within 15% of any activated fraction

151   measured at the three highest supersaturations. This indicates that the activation fraction

152   did not reach a plateau even at the highest supersaturations sampled, and therefore E is

153   not well constrained by the activation spectrum.

154   3. The residue of the fit is greater than 0.1. This indicates relatively poor fit, which

155   represented less 1% of the activation spectra.

156   4. The fitted E is less than 0.5, indicating external mixtures with substantial fraction of fresh

157   black carbon and primary organic aerosols emitted by the generator, vehicles, and grass

158   cutting activities at or near the site.

159   For the one-year measurement period, 6.5 % of the total activation curves were removed by

160   the above data quality filters.

161

162   **3.4 Deriving average particle hygroscopicity and hygroscopicity dispersion from activation**
163   **spectrum**

164   For particles with the same size and composition (i.e., hygroscopicity), a step increase of R_a

165   from 0% to 100% with increasing supersaturation is expected because all particles would have

166   the identical critical supersaturation (S_c).   The measurements of ambient aerosols show more

167   gradual increase in R_a (i.e., instead of a step change), suggesting heterogeneity in particle S_c. The

168   heterogeneity in particle S_c, as described by σ_s is due to a combination of width of DMA transfer

169   function (particles classified by a DMA do not have exactly the same size), instrument non-

170   idealities, and the heterogeneity in particle hygroscopicity. The value of σ_s due to the

171   heterogeneity in particle hygroscopicity alone can be estimated by:

172    $$\sigma_s = \sqrt{\sigma_{s,\mathrm{m}}^2 - \sigma_{s,\mathrm{AS}}^2} \qquad\qquad\qquad (S1)$$

173   Where $\sigma_{s,\mathrm{m}}$ and $\sigma_{s,\mathrm{AS}}$ are the values corresponding to the ambient measurement and the calibration

174   using ammonium sulfate, respectively. Particle critical supersaturation S_c is related to

175   hygroscopicity κ by (Petters and Kreidenweis, 2007):

176    $$S_c(\kappa) = \left(\frac{4A^3}{27D_p^3\kappa}\right)^{1/2} ,$$
$$A = \frac{4\sigma_w M_w}{RT\rho_w} \qquad\qquad\qquad (S2)$$

177   Where D_p is the particle diameter, M_w, ρ_w and σ_w are the molecular weight, density and surface

178   tension of water, respectively. The probability distribution function of particle hygroscopicity

179    $p(\kappa)$ can be derived as the following:

180    $$p(\kappa) = -\frac{dR_a\left(S_c(\kappa)\right)}{d\kappa} \qquad\qquad\qquad (S3)$$

181   Where R_a is the fitted active spectrum with σ_s adjusted using Eq. (S1). The dispersion of κ, which

182   describes the heterogeneity of hygroscopicity for activated particles, is given by (Mei et al.,

183   2013):

184    $$\sigma(\kappa)/\overline{\kappa_{\mathrm{CCN}}} = \left[\exp\left(4\sigma_s^2\right) - 1\right]^{1/2} \qquad\qquad\qquad (S4)$$

185 where $\sigma(\kappa)$ and $\overline{\kappa_{CCN}}$ are the standard deviation and average value of the hygroscopicity for

186 activated particles.

187 It is worth noting that because of the skewness of the lognormal distribution, the average particle

188 hygroscopicity $\overline{\kappa_{CCN}}$ is higher than κ^*, which corresponds to the fitted S^*, and represents the

189 median hygroscopicity of activated particles (Fig. S6). The difference between $\overline{\kappa_{CCN}}$ and κ^*

190 becomes significant at high σ_s values (Fig. S7). In this study, $\overline{\kappa_{CCN}}$ is derived from the

191 probability density function using the following equation:

$$192 \quad \overline{\kappa_{CCN}} = \frac{\int_0^{0.65} \kappa \cdot p(\kappa) d\kappa}{\int_0^{0.65} p(\kappa) d\kappa} \qquad (S5)$$

193 The upper limit of the integration is limited to 0.65, which reflects the maximum particle

194 hygroscopicity expected at the T3 site. The organic hygroscopicity is derived from the average

195 particle hygroscopicity $\overline{\kappa_{CCN}}$ and average chemical composition.
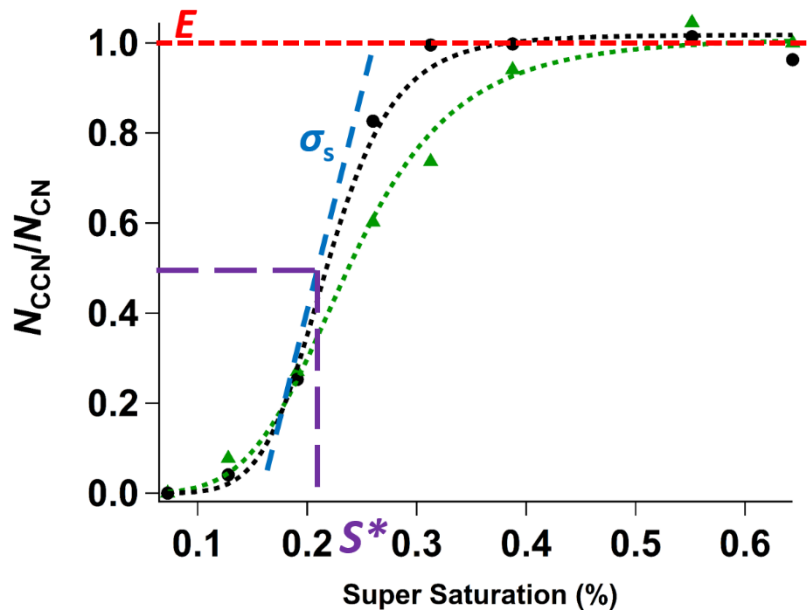
196

197 Figure S6: Sample activation spectra for particles with diameter of 142 nm. The black dots and
198 green triangles represent spectra with a low dispersion ($\sigma_s = 0.2$; $\sigma(\kappa)/\overline{\kappa_{CCN}} = 0.4$) and a much
199 higher dispersion ($\sigma_s = 0.4$; $\sigma(\kappa)/\overline{\kappa_{CCN}} = 0.9$), respectively.
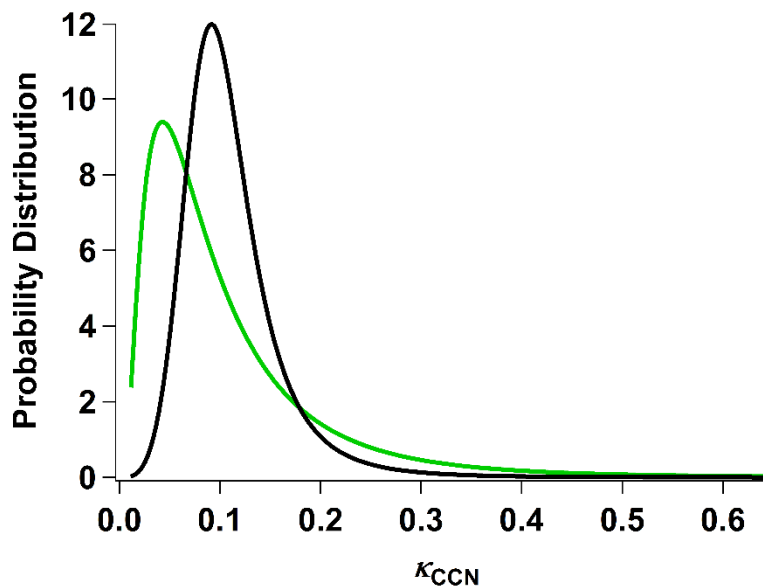
200

201 Figure S7: Probability density distributions of particle hygroscopicity derived from the fitted
202 activation spectra shown in Figure S6. As dispersion increases, the distribution becomes
203 increasingly asymmetric, and the difference between $\overline{\kappa_{CCN}}$ and κ^* increases.

4 Aerosol composition derived from AMS and rBC measurements

4.1 Bulk and size-resolved mass concentration of aerosol species

Given the very low aerosol mass concentration in the Amazon basin, the signal to noise ratio of particle time-of-flight (P-ToF) mode measurement was not sufficient to directly provide size resolved species mass concentrations for individual CCN activation spectrum. Instead, the size resolved species mass concentrations were constructed by combing the bulk mass concentrations measured in MS mode, which have higher signal to noise ratio, and P-ToF mode size resolved species mass distributions averaged over extended time periods. For both IOPs, the bulk organics mass fraction was derived from MS mode portion of individual AMS measurement. Based on the bulk organic mass fraction, measurements during IOP1 were then classified into three groups with equal number of measurements, and the characteristic mass size distribution of each species (i.e., organics, SO_4, NO_3, and NH_4) was averaged from P-ToF measurements within each group. For IOP2, the measurements were classified into three groups each for day and night periods based on the bulk aerosol organic mass fraction, and the mass size distribution of each species was averaged from P-ToF measurements in each of the six groups. The average mass size distributions of the four species for the three groups during the daytime of IOP2 are shown in Fig. S8 as examples. The underlying assumption is that observed aerosols exhibiting similar bulk composition (i.e., organic mass fraction) during the IOPs also had species mass size distributions with the same shapes. The vacuum aerodynamic diameter (D_{va}) measured by the AMS was converted to particle mobility diameter (D_m) and volume equivalent diameter (D_v) using the particle density with the assumption of spherical particles, which is reasonable given most of the aerosol observed at T3 site were quite aged. The average densities were calculated using the approach described in Kuwata et al. (2012), and were 1.45 µg m^3 and 1.47 during IOP 1 and 2, respectively. In this study, unless otherwise indicated, particle diameter D_p represents

228   the mobility diameter (D_m), which is equivalent to the volume average diameter given the

229   assumption of spherical particles.
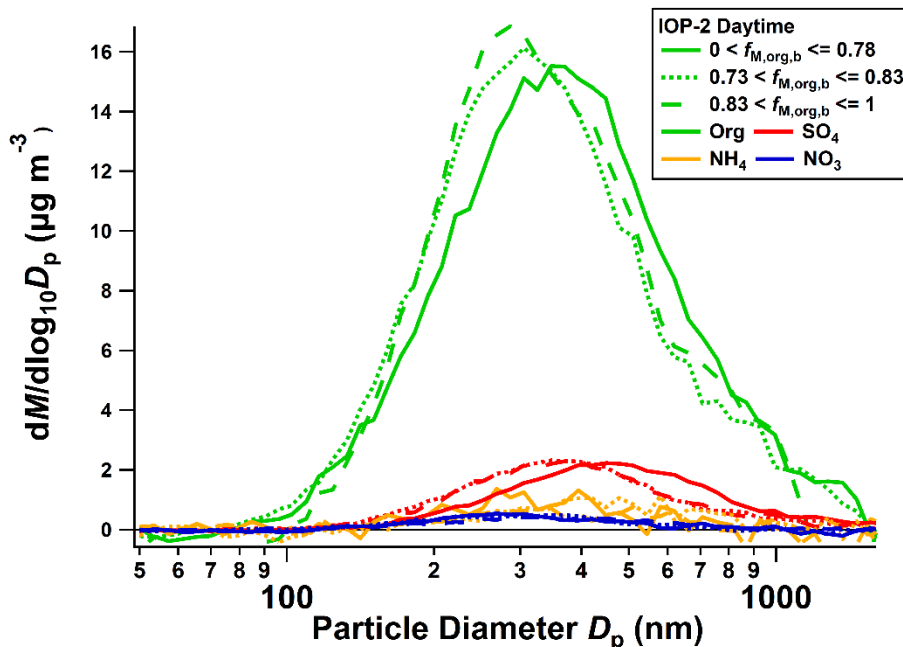
230

231   Figure S8: Size resolved mass concentrations of organics, SO$_4$, NO$_3$, and NH$_4$ averaged from P-
232   ToF measurements for each of three groups during the day time of IOP2 (dry season). The three
233   groups were classified based on bulk organics mass fraction ($f_{M,org}$).

234

235   For individual AMS measurements, the size resolve chemical composition was then

236   derived as follows: the organic mass concentration at the particle diameter of CCN

237   measurements, $m_{org}\left(D_p\right)$, was calculated as:

238    $$m_{org}\left(D_p\right)=M_{org,b}\times\frac{\bar{m}_{org}\left(D_p\right)}{\int_{D_{p,min}}^{D_{p,max}}\bar{m}_{org}\left(D_p^{'}\right)d\log D_p^{'}}\qquad\text{(S6)}$$

239   where $M_{org,b}$ is the bulk organic mass concentration from MS mode measurement, $\bar{m}_{org}(D_p)$ is

240   the average organic mass size distribution with respect to $\log D_p$, $D_{p,max}$ and $D_{p,min}$ are the

241 maximum and minimum diameters of the average mass size distribution. Using the same

242 approach, the mass concentration of SO_4^{2-}, NO_3^-, and NH_4^+ at specific D_p are calculated using

243 the corresponding average mass size distributions. Mass concentration for black carbon

244 $m_{rBC}(D_p)$ is derived with the assumption that the mass size distribution of rBC has the same

245 shape of the total mass size distribution:

$$246 \quad f_{M,rBC} = \frac{M_{rBC,b}}{M_{total,b}} = \frac{m_{rBC}(D_p)}{m_{SO_4^{2-}}(D_p) + m_{NO_3^-}(D_p) + m_{NH_4^+}(D_p) + m_{org}(D_p) + m_{rBC}(D_p)} \quad (S7)$$

247 where $f_{M,rBC}$ is the bulk mass fraction of refractory black carbon, $M_{rBC,b}$ and $M_{total,b}$ are the

248 bulk rBC and total aerosol mass concentrations, respectively. From Eq. (S7), $m_{rBC}(D_p)$ can be

249 derived as:

$$250 \quad m_{rBC}(D_p) = \frac{f_{M,rBC}\left[m_{SO_4^{2-}}(D_p) + m_{NO_3^-}(D_p) + m_{NH_4^+}(D_p) + m_{org}(D_p)\right]}{\left(1 - f_{M,rBC}\right)} \quad (S8)$$

251 The fractional chemical composition at the size of CCN measurement D_p was then derived from

252 the species mass concentrations calculated above. While not perfect, this approach allowed us to

253 take both the temporal variation and size dependence of species mass concentrations into

254 consideration when deriving particle composition at the sizes of CCN measurements. This is

255 important because the organic volume fraction, required to derive the organic hygroscopicity was

256 often much higher at the sizes of CCN measurements than that based on the bulk measurements.

257

258

259 **4.2 Sulfate and nitrate**

260   Outside of the IOP periods, particle composition was derived from ACSM data, and the

261   retrieval of organonitrate mass concentration is not available. In addition, the detection limit of

262   NH_4^+ for the ACSM is very high, such that the measurement of NH_4^+ mass concentration was

263   too noisy for determining aerosol ionic balance. The sensitivity of derived κ_{org} to the assumption

264   on nitrate was examined using the AMS data from the two IOPs to inform the appropriate

265   assumptions for the analysis outside the IOP periods. Organic hygroscopicity was calculated

266   using three different approaches: (1) the approach based on the retrievals of both inorganic and

267   organic nitrate mass concentrations from AMS, as described in section 3.2 of the main text, (2)

268   all NO_3^- was assumed from NH_4NO_3 and all sulfate from ammonium sulfate, and (3) all NO_3^-

269   was from organonitrate with all sulfate from ammonium sulfate. κ_{org} derived using the three

270   different assumptions are shown in Figure S9 for both IOPs. When all NO_3^- is assumed from

271   organonitrate (i.e., approach 3), the derived κ_{org} values are very close to those based on retrieved

272   organonitrate and inorganic nitrate concentrations from AMS data (i.e., approach 1). As a result,

273   for measurements outside of the two IOPs when only ACSM measurements are available, all

274   measured NO_3^- was assumed from organonitrate and sulfate was assumed from ammonium

275   sulfate.

276
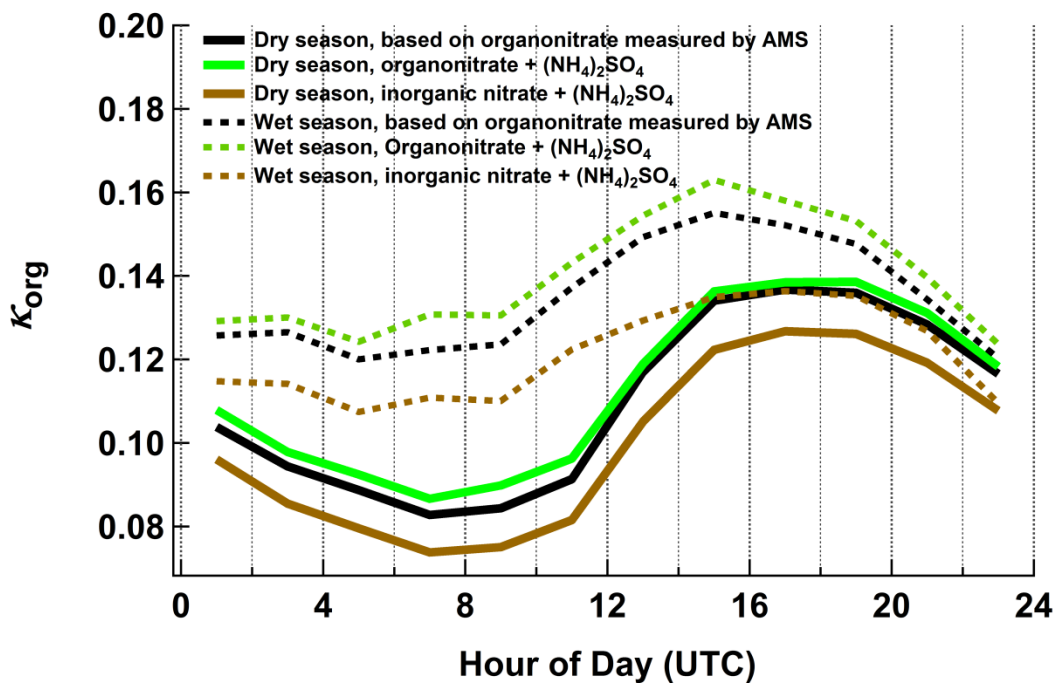
277

278 Figure S9: Diel variations of organic hygroscopicity derived using the three different
279 assumptions on nitrate described in the text (i.e., mixed inorganic/organic nitrates, all organic
280 nitrate, and all inorganic nitrate).

281

282
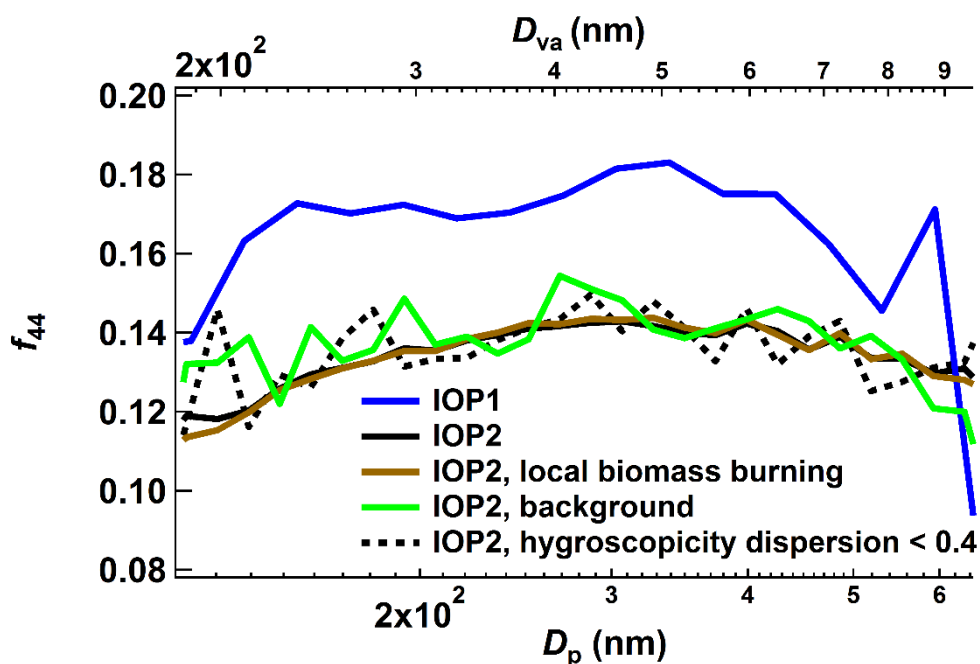
Figure S10: Size dependence of the fraction of the organic mass at m/z = 44 (f_{44}), which is indicative of the extent of oxidation. The f_{44} averaged during IOP1 was essentially independent of particle diameter D_p from 140 to 400 nm, a size range that dominated bulk organic mass concentration and encompasses the diameters of CCN measurements (i.e., 142 and 171 nm). During the IOP2, f_{44} averaged for all data and local biomass burning air mass type showed a clear dependence on D_p. In comparison, f_{44} averaged for the background condition and the periods with low hygroscopicity dispersion ($\sigma_{\bar{\kappa}}/\bar{\kappa} < 0.4$) during IOP2 had lower signal to noise ratio due to the low mass loading, but were largely independent of particle size.

291

292 **Tables**

293 Table S1: Particle diameter classified by the DMA and the corresponding diameters for doubly
294 and triply charged particles. Diameters in the parenthesis represent the measurements (if
295 available) used to correct the contribution of doubly and triply charged particles to the measured
296 activation fractions.

DMA classified singly charged particles, D_p (nm)	Doubly charged particles D_p (nm)	Triply charged particles D_p (nm)
51	75 (75)	94 (94)
75	112 (112)	142 (142)
94	142 (142)	182(171)
112	171 (171)	222 (222)
142	221 (222)	293 (N/A)
171	272 (N/A)	365 (N/A)
222	364 (N/A)	498 (N/A)

297

298

299

300 Table S2: Criteria used to classify air mass type for different seasons. The threshold values of CN
301 and CO concentrations used to identify background conditions are the mean plus one standard deviation
302 of respective measurements at the background sites T0a and T0t.

Air mass type	Season			
	Wet/Wet 2	Transition 1	Dry	Transition 2
Background	$CN<500$ cm^{-3} $CO<0.14$ ppm $NO_y<1.5$ppbv	$CN<900$ cm^{-3} $CO<0.14$ ppm $NO_y<1.5$ppbv	$CN<1500$ cm^{-3} $NO_y<1.5$ppbv	$CN<1500$ cm^{-3} $NO_y<1.5$ppbv
Urban Pollution	$CN>500$ cm^{-3} $*f_{<70}>0.45$	$CN>900$ cm^{-3} $f_{<70}>0.45$	$CN>1500$ cm^{-3} $f_{<70}>0.45$	$CN>1500$ cm^{-3} $f_{<70}>0.45$
Local biomass burning	$CN>500$ cm^{-3} $f_{<70}<0.45$ $CO>0.14$ ppm	$CN>900$ cm^{-3} $f_{<70}<0.45$ $CO>0.14$ ppm	$CN>1500$ cm^{-3} $f_{<70}<0.45$	$CN>1500$ cm^{-3} $f_{<70}<0.45$
Site Contamination	$BC>1$ µg m^{-3} $CN>10^4$ cm^{-3}	$BC>1$ µg m^{-3} $CN>10^4$ cm^{-3}	$BC>1$ µg m^{-3} $CN>10^4$ cm^{-3}	$BC>1$ µg m^{-3} $CN>10^4$ cm^{-3}

303 * $f_{<70}$: number fraction of particles with diameters less than 70 nm, derived from SMPS
304 measurement.

305

306

307

308

309

310

311

312

313

314

315

316

317   Table S3: Classification of air masses for size resolved CCN measurements at 112, 142, and 171
318   nm, and relevant measurements (CN, CO, SMPS, rBC) averaged to 5-min intervals.

Season	Classification	Percentage of air mass types	
		Size resolved CCN	Relevant measurements
Wet Season 2014	Background	10.2%	17.5%
	Urban Pollution	65.1%	63.7%
	Local Biomass Burning	0.7%	0.6%
	Site Contamination	1.1%	1.3%
	Invalid CCN spectra Fit[#]	12.5%	N/A
	Unclassified[$]	10.5%	17.0%
Transition Season 1	Background	8.9%	11.8%
	Urban Pollution	59.2%	59.1%
	Local Biomass Burning	3.4%	3.6%
	Site Contamination	1.0%	1.2%
	Invalid CCN spectra Fit[#]	4.0%	N/A
	Unclassified[$]	23.6%	24.2%
Dry Season	Background	7.9%	9.7%
	Urban Pollution	14.4%	16.4%
	Local Biomass Burning	68.1%	58.6%
	Site Contamination	1.3%	1.1%
	Invalid CCN spectra Fit[#]	2.9%	N/A
	Unclassified[$]	5.5%	14.3%
Transition Season 2	Background	26.5%	26.9%
	Urban Pollution	11.0%	10.1%
	Local Biomass Burning	50.4%	53.8%
	Site Contamination	1.7%	2.0%
	Invalid CCN spectra Fit[#]	3.3%	N/A
	Unclassified[$]	7.0%	7.3%
Wet Season 2015	Background	8.1%	12.6%
	Urban Pollution	39.6%	41.2%
	Local Biomass Burning	25.6%	24.5%
	Site Contamination	0.8%	0.9%
	Invalid CCN spectra Fit[#]	8.3%	N/A
	Unclassified[$]	17.6%	20.8%
Mar 2014 - Mar 2015	Background	12.4%	16.5%
	Urban Pollution	38.5%	41.2%
	Local Biomass Burning	28.4%	24.7%
	Site Contamination	1.2%	1.3%
	Invalid CCN spectra Fit[#]	6.5%	N/A
	Unclassified[$]	13.0%	16.3%

319

320 # An invalid fit of the CCN actiation spectrum (Sec. S3.2)
321 $ One or more of the measurements (CN, SMPS, CO, rBC) neede to classify air mass is missing
322 or air mass is not classifed as one of the four types using the the criteria described in Table S2.

323 **References**

324 Kuwata, M., Zorn, S. R., and Martin, S. T.: Using Elemental Ratios to Predict the Density of
325 Organic Material Composed of Carbon, Hydrogen, and Oxygen, Environmental Science &
326 Technology, 46, 787-794, 2012.

327 Lance, S., Nenes, A., Medina, J., and Smith, J. N.: Mapping the Operation of the DMT
328 Continuous Flow CCN Counter, Aerosol Science and Technology, 40, 242-254, 2006.

329 Mei, F., Hayes, P. L., Ortega, A., Taylor, J. W., Allan, J. D., Gilman, J., Kuster, W., de Gouw, J.,
330 Jimenez, J. L., and Wang, J.: Droplet activation properties of organic aerosols observed at an
331 urban site during CalNex-LA, Journal of Geophysical Research: Atmospheres, 118, 2903-2917,
332 2013.

333 Petters, M. D. and Kreidenweis, S. M.: A single parameter representation of hygroscopic growth
334 and cloud condensation nucleus activity, Atmos. Chem. Phys., 7, 1961-1971, 2007.

335 Roberts, G. C. and Nenes, A.: A Continuous-Flow Streamwise Thermal-Gradient CCN Chamber
336 for Atmospheric Measurements, Aerosol Science and Technology, 39, 206-221, 2005.

337 Rose, D., Gunthe, S. S., Mikhailov, E., Frank, G. P., Dusek, U., Andreae, M. O., and Poschl, U.:
338 Calibration and measurement uncertainties of a continuous-flow cloud condensation nuclei
339 counter (DMT-CCNC): CCN activation of ammonium sulfate and sodium chloride aerosol
340 particles in theory and experiment, Atmos. Chem. Phys., 8, 1153-1179, 2008.

341 Shilling, J. E., King, S. M., Mochida, M., Worsnop, D. R., and Martin, S. T.: Mass Spectral
342 Evidence That Small Changes in Composition Caused by Oxidative Aging Processes Alter
343 Aerosol CCN Properties, The Journal of Physical Chemistry A, 111, 3358-3368, 2007.

344 Wiedensohler, A.: An approximation of the bipolar charge distribution for particles in the
345 submicron range, J. Aerosol Sci., 19, 387-390, 1988.

346

347